

Liquid plug formation in an airway closure model

F. Romanò *

Department of Biomedical Engineering, University of Michigan, 2123 Carl A. Gerstacker Building,
2200 Bonisteel Boulevard, Ann Arbor, Michigan 48109-2099, USA
and Univ. Lille, CNRS, ONERA, Arts et Metiers ParisTech, Centrale Lille, FRE 2017-LMFL-Laboratoire
de Mécanique des Fluides de Lille–Kampé de Fériet, F-59000, Lille, France

H. Fujioka

Center for Computer Science, Tulane University, 6823 St. Charles Avenue,
New Orleans, Louisiana 70118, USA

M. Muradoglu

Department of Mechanical Engineering, Koc University, Rumeli Feneri Yolu, 80910 Sariyer, Istanbul, Turkey

J. B. Grotberg

Department of Biomedical Engineering, University of Michigan, 2123 Carl A. Gerstacker Building,
2200 Bonisteel Boulevard, Ann Arbor, Michigan 48109-2099, USA



(Received 16 April 2019; published 24 September 2019)

The closure of a human lung airway is modeled as an instability of a two-phase flow in a pipe coated internally with a Newtonian liquid. For a thick enough coating, the Plateau-Rayleigh instability creates a liquid plug which blocks the airway, halting distal gas exchange. Owing to a bifrontal plug growth, this airway closure flow induces high stress levels on the wall, which is the location of airway epithelial cells. A parametric numerical study is carried out simulating relevant conditions for human lungs, in either ordinary or pathological situations. Our simulations can represent the physical process from pre- to postcoalescence phases. Previous studies have been limited to precoalescence only. The topological change during coalescence induces a high level of stress and stress gradients on the epithelial cells, which are large enough to damage them, causing sublethal or lethal responses. We find that postcoalescence wall stresses can be in the range of 300% to 600% greater than precoalescence values and so introduce an important source of mechanical perturbation to the cells.

DOI: [10.1103/PhysRevFluids.4.093103](https://doi.org/10.1103/PhysRevFluids.4.093103)

I. INTRODUCTION

Respiratory airways are a branching network of tubular structures coated internally with a liquid film. As shown in Fig. 1, an infinitesimally small varicose perturbation induces a Plateau-Rayleigh instability driven by the surface tension at the air-liquid interface. Under certain conditions, the minimum radial distance from the tube centerline to the interface, $R_{\min}(t)$, decreases toward zero during the instability. We refer to this as the *precoalescence phase* shown in Fig. 1 for $t = t_1$, t_2 with $R_{\min}(t_2)$ being indicated. If the thickness of the undisturbed liquid film, h , scaled by the airway radius, a , exceeds a critical value of h_c/a , R_{\min} can reach zero at $t = t_c$, i.e., coalescence.

*frrmano@umich.edu

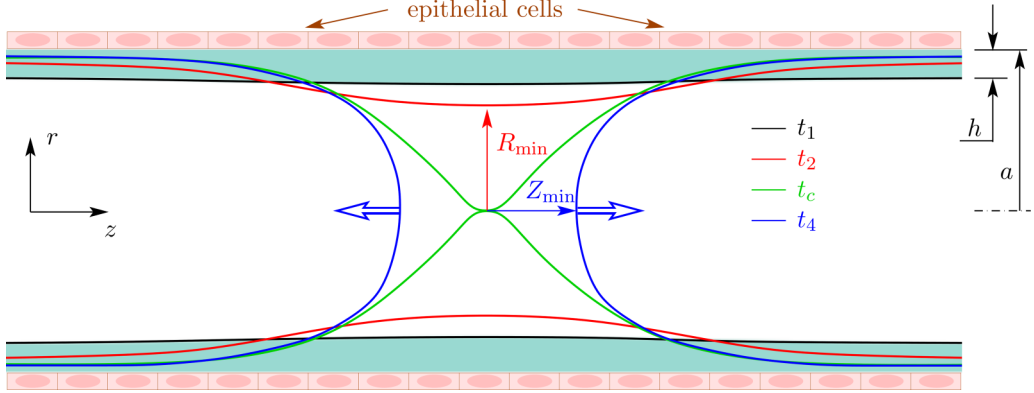


FIG. 1. Schematic of the airway closure process. The air-liquid interface is depicted at four instants of time: for $t = t_1$ the interface is slightly deformed, for $t = t_2$ the deformation has increased because of the Plateau-Rayleigh instability, for $t = t_c$ it coalesces while undergoing a topological change, and for $t = t_4$ the newly formed liquid plug undergoes a bifrontal growth.

The coalescence leads to a topological change, as shown. This is quickly followed by the *postcoalescence phase* forming a liquid plug by means of a *bifrontal growth*, t_4 . Because of the topological change, now the minimum distance to the interface is measured in the axial direction, $Z_{\min}(t)$, as shown in Fig. 1 for $Z_{\min}(t_4)$. This phenomenon is known as *airway closure*, and a plugged airway prevents gas exchange for regions of the lung distal to it. Due to flexibility of the airways [1,2], a direct consequence of the airway closure may be the collapse of the airway, which contributes to heterogeneous ventilation [3].

Airway closure is usually associated with surfactant deficiency or dysfunction, accumulation of liquid from infections or edema, or mucus hypersecretion along the airway. Typical lung diseases involved include asthma [4], pneumonia [5], bronchiolitis [6], cystic fibrosis [7], chronic obstructive pulmonary disease (COPD [8]), and acute respiratory distress syndrome (ARDS [9]), just to name a few. It generally occurs in small airways near the end of expiration. The lung volume at which closure initiates is called the closing volume, a routine pulmonary function test which varies with disease, age, and gender [10,11]. For an upright lung in gravity, the lower regions have compressed airway diameters from the weight of the lung above, so closure tends to occur there initially. It is therefore expected that, under microgravity conditions, airway closure occurs more homogeneously posing a potential risk, see [12–14].

For a clean interface in a rigid pipe, the critical film thickness is $h_c/a \approx 0.12$ [15]. This is the minimum film thickness, normalized with the airway radius, such that the interfacial instability induces the airway closure within one breathing cycle. Several studies have investigated models of the pre-coalescence closure instability under additional circumstances, including the effects of surfactant, viscoelasticity, nonaxisymmetry, and wall flexibility. The effects of surfactants have been experimentally studied in capillary tubes in Refs. [16,17], which pointed out that a surfactant can increase h_c/a and decrease the growth rate, which increases the closure time, t_c . Theoretical and computational models based on lubrication theory [17,18] and full Navier-Stokes equations [19] also confirm these findings. The Marangoni stresses induced by uneven distribution of interfacial surfactant concentration oppose the closure flow. Halpern *et al.* [20], using lubrication theory, showed that viscoelasticity does not strongly affect the critical film thickness h_c/a , and for $h_c/a < 0.119$ airway closure does not occur within a breathing cycle. On the other hand, if $14\% \leq h/a \leq 18\%$, increasing the Weissenberg number speeds up the growth rate when the viscoelastic fluid exhibits a shear-thinning behavior. The effect of wall compliance has been studied in Refs. [18,21]. They showed that the airway wall deforms to narrow the tube and reduce the radius of curvature for the air-liquid interface, thereby enhancing the instability. Heil *et al.* [22]

demonstrated how nonaxisymmetric mechanical and hydrodynamic instabilities may lead to the formation of a plug at lower h_c/a than predicted by the axisymmetric models. Prevention of closure by oscillating the core fluid axially was explored in Ref. [23], where nonlinear saturation of the instability is reached with growth during the turnaround phase balanced by decay during the stroke phase when fluid is deposited back onto the wall, a “reversing butter knife.” These previous studies form a basis and motivate the present work, which does not only cover the pre-coalescence, but also extends to coalescence and postcoalescence phases.

Similar topological changes have been extensively studied for liquid bridges, snapping liquid columns, and liquid jets [24–26]. Even if much attention has been paid to understand the capillary instability for freely suspended liquids, remarkably less effort has been spent on interfacial instabilities of liquid-lined pipes [27–30], where the tube boundaries play a major role. The pioneering work of Newhouse and Pozrikidis [31] investigated the liquid plug formation in a liquid lined pipe, when the two fluids involved have the same viscosity. The focus of their study was on the liquid thread which forms right before coalescence and undergoes capillary instability giving rise to formation of satellite droplets after the closure event. A thorough investigation about liquid-lined pipes has recently been conducted by Dietze and Ruyer-Quil [32]. However, the relevance of the topological change on the wall stresses has almost been ignored, so far. Our study focuses on this aspect, advancing the understanding of liquid plug formation in coated pipes and paying special attention to the stresses on the pipe wall during the whole plug formation phenomenon.

Reviews of respiratory airway closure, liquid plug propagation, and rupture appear in Refs. [14,33–35], and a recent paper of Grothberg [36] points out how mechanical stresses and strains can cause lung disease or injury. While cell injury and its correlation to fluid stresses have been explored for plug propagation and rupture, less attention has been paid to similar issues for airway closure flows; see the epithelial cells in Fig. 1. Our previous experimental and numerical investigations [37,38] have shown that the stress levels due to the capillary instability are also important. The numerical results of Ref. [38], limited to pre-coalescence, agree well with the experimental data of Bian *et al.* [37] who also provided measurements for the postcoalescence phases. In this work, we present a computational study for the entire closure process, from pre- to postcoalescence. Moreover, the effects of the viscosity of the liquid layer and of surface tension between liquid and gas have not been thoroughly considered in the previous airway closure models, even though the viscosity of mucus can range over three orders of magnitude. In this paper we investigate the effects of liquid viscosity and surface tension for various values of the liquid layer thicknesses, considering the range of parameters of physiological relevance in the human respiratory system. We simulate the whole process of plug formation and validate our results using the experimental data of Ref. [37]. The remainder of the paper is organized as follows: In Sec. II the formulation of the mathematical model is discussed, and in Sec. III we briefly describe the numerical approach used in the present study. The results are presented and discussed in Sec. IV, and finally conclusions are drawn in Sec. V.

II. PROBLEM FORMULATION

The airway closure model employed in this study consists of a cylindrical rigid tube of radius a and length L , internally coated with a Newtonian liquid film of average thickness h , constant dynamic viscosity μ_L , and density ρ_L . The liquid film is surrounded by a gas of constant dynamic viscosity μ_G and density ρ_G at the core of the pipe as shown in Fig. 2. The surface tension, σ , between liquid and gas is assumed to be constant.

The interface between the two immiscible phases is assumed to be perturbed from its average thickness such that its radial location is initially located at

$$r = R_1 = a - h[1 - 0.1 \times \cos(2\pi z/L)], \quad (1)$$

where z and r denote the axial and radial coordinate, respectively.

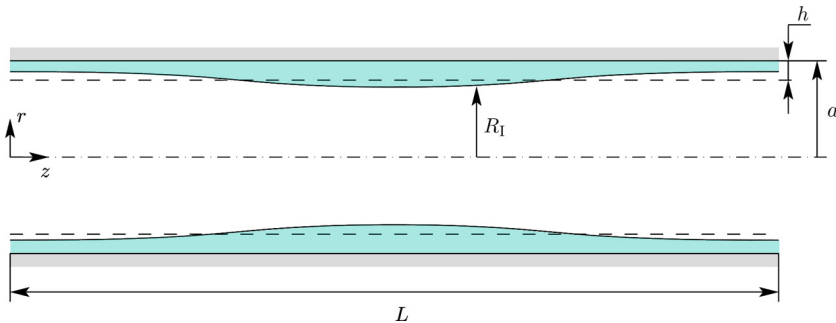


FIG. 2. Schematic of the geometry of the airway model: the rigid tube has radius a , length L , is coated by a liquid film (light blue) of average thickness h and surrounded by a gas core. The interface is initially located at a distance R_1 from the axis of the pipe.

Making use of a capillary scaling, i.e., nondimensionalizing length, time, pressure, and velocity with a , $\mu_L a / \sigma$, σ / a , and σ / μ_L , respectively, the nondimensional equations for a two-phase flow can be written in the single-field formulation as [39,40]

$$\partial_t \tilde{\varrho} + \mathbf{u} \cdot \nabla \tilde{\varrho} = 0, \quad (2a)$$

$$\nabla \cdot \mathbf{u} = 0, \quad (2b)$$

$$\text{La} \tilde{\varrho} (\partial_t \mathbf{u} + \mathbf{u} \cdot \nabla \mathbf{u}) = -\nabla p + \nabla \cdot [\tilde{\mu} (\nabla \mathbf{u} + \nabla^T \mathbf{u})] + \chi n \delta_s, \quad (2c)$$

where $\mathbf{u} = (u_r, u_\phi, u_z)$ and p denote the velocity and pressure field, respectively, $\chi = \nabla \cdot \mathbf{n}$ is the total local curvature of the interface, \mathbf{n} the outward unit normal at the interface, δ_s is the surface Dirac δ function, which is nonzero only along the two-phase interface, and $\tilde{\varrho}$ and $\tilde{\mu}$ are the variable density and dynamic viscosity field in the single-field approach, which include the effect of the gas-to-liquid density and dynamic viscosity ratio (ϱ and μ , respectively), i.e., in the liquid phase $(\tilde{\varrho}, \tilde{\mu}) = (1, 1)$ whereas in the gas phase $(\tilde{\varrho}, \tilde{\mu}) = (\varrho, \mu)$. Hence, the nondimensional numbers resulting from the momentum equation are the Laplace number La , the gas-to-liquid density ratio ϱ , and the gas-to-liquid dynamic viscosity ratio μ . Moreover, two additional nondimensional groups are introduced to characterize the geometry of our configuration: the length-to-radius aspect ratio λ and the rescaled average film thickness ε . The relevant nondimensional parameters can be summarized as

$$\text{La} = \frac{\rho_L \sigma a}{\mu_L^2}, \quad \varrho = \frac{\rho_G}{\rho_L}, \quad \mu = \frac{\mu_G}{\mu_L}, \quad \lambda = \frac{L}{a}, \quad \varepsilon = \frac{h}{a}. \quad (3)$$

To close the mathematical problem, periodic boundary conditions are used in axial direction, while no-slip and no-penetration are enforced at the tube wall:

$$\mathbf{u}(z=0) = \mathbf{u}(z=\lambda), \quad \mathbf{u}(r=1) = \mathbf{0}. \quad (4)$$

III. NUMERICAL SIMULATIONS

The mathematical problem defined in the previous section is tackled assuming that the film closure can be modeled as an axisymmetric phenomenon, i.e., $\partial_\phi = 0$, $u_\phi = 0$. Simulations are performed using a volume-of-fluid (VOF) method implemented in the open-source code BASILISK [41]. In this method, a second-order finite volume discretization is adopted in space, and the time integration is carried out by means of a second-order pressure-correction projection method. A semi-implicit approach is used, which discretizes the viscous terms implicitly and the convective terms explicitly using the Bell-Collella-Glaz advection scheme [42]. The single-field model is the natural setting for applying the *volume-of-fluid* (VOF) method. VOF belongs to the front-capturing methodologies and employs a fraction field $f(r, z, t)$ which equals 1 in the liquid and 0 in the gas

TABLE I. Grid convergence for $La = 100$, $\mu = 0.0015$, $\varrho = 0.001$, $\lambda = 6$, $\varepsilon = 0.25$. The simulations are carried out for a final time $t = 1000$.

N_r	N_z	$\max_t (\Delta p_w)$	$\max_t (\Delta \tau_w)$
11	64	1.2766	0.3627
21	128	1.3887	0.4608
43	256	1.3571	0.5163
86	512	1.3488	0.5204

and ranges between these two values across the liquid-gas interface. Hence, the fraction field is here intended as the volume fraction of liquid in a given computational cell, and it is used to define the variable material properties in the single-field approach [43,44]:

$$\tilde{\varrho}[f(r, z, t)] = f + (1 - f)\varrho, \quad (5a)$$

$$\tilde{\mu}[f(r, z, t)] = f + (1 - f)\mu. \quad (5b)$$

The fraction field is simply advected by the flow velocity:

$$\partial_t f + \nabla \cdot (f\mathbf{u}) = 0. \quad (6)$$

A piecewise-linear geometrical VOF method [45] is used to solve (6), where the interface is represented as a piecewise linear function within each computational cell. A staggered approach is employed to achieve a second-order accuracy in time, as described in Ref. [44]. Once it is advected, the local unit vector is computed using the Mixed-Youngs-Centered method [46] and the material properties are set in each phase according to (5). Finally, the surface-tension term, which appears in the momentum equation of a single-field model, has to be discretized. Inaccurate discretization of a surface tension term typically results in parasitic currents (see Refs. [40,47]), a common problem for all one-field approaches including the front-tracking and front-capturing methods (e.g., phase-field and level sets methods). In the following, the approach of Popinet [44] is employed, combining a height-function estimator for the interface curvature and a balanced-force surface-tension discretization. It has been shown that such a combination reduces the parasitic currents significantly and yields a second-order spatial accuracy for challenging benchmark cases (see Ref. [44]).

The solution is computed on a staggered grid, where the pressure and the velocity fields are located at the cell centers and at the cell faces, respectively. The other scalar fields such as volume fraction and material properties are also located at the cell centers. The computational mesh is a Cartesian grid designed for capturing the quantities of major interest in our study including the pressure (p_w) and the shear stress (τ_w) on the tube wall. A grid convergence study is first performed, and the results are reported in Table I, where N_r and N_z denote the number of grid cells in the radial and axial directions, respectively. In Table I, $\Delta p_w = \max(p_w) - \min(p_w)$ and $\Delta \tau_w = \max(\tau_w) - \min(\tau_w)$ are the maximum difference in the pressure and the shear stress on the wall, respectively. All the following simulations are computed considering the finest grid, which consists of 512 cells in the z and 86 cells in the r direction.

IV. RESULTS AND DISCUSSION

In this study we investigate the effect of three nondimensional groups: the Laplace number La , the relative film thickness, ε , and the gas-to-liquid dynamic viscosity ratio, μ . The parameters are chosen to characterize the physical phenomenon for airway closures occurring at the ninth to tenth branching generations in the adult human lungs. Both normal and pathological conditions are considered. Simulations are performed to examine the time evolution of the instability and

determine the associated velocities and the wall stresses. The latter are of major relevance for the epithelial cells in the modeled biological system.

A. Validation

The airway model we numerically simulate is first validated comparing the computational results with the experimental measurements of Bian *et al.* [37], who report an experimental study of a two-liquid closure instability in a pipe, whose inner radius equals 0.058 cm, lined with 96% glycerol film ($\mu_L = 5.498$ poise and $\rho_L = 1.251$ g cm⁻³) of initial average thickness $\varepsilon = 0.23$. The core fluid is silicone oil yielding $\mu = 0.01$ and $\varrho \approx 0.95$.

The surface tension between the two fluids is $\sigma = 30$ dyn cm⁻¹. The nondimensional parameters of interest are $La = 0.072$, $\mu = 0.01$, $\varrho = 0.95$, and $\lambda = 9.2$. As pointed out by Tai *et al.* [38], the closure time is an unreliable validation criterion for numerical models, since it is strongly influenced by the initial amplitude of the perturbation which cannot be experimentally measured with the required accuracy. Hence, following Ref. [38], we set the initial disturbance amplitude to $5\%\varepsilon$ [$10\%\varepsilon$ is used in all the other simulations; see (1)] and carry out our comparison with the bench-top experiments in Ref. [37]. The experimental results are shifted in time to match the experimental t_c with the numerical t_c .

In Fig. 3 the numerical results are compared with the experimental visualizations for the evolution of the interface during the plug formation process including pre- and postcoalescence phase. Reconstructing the interface shape by the piecewise-linear geometrical VOF method [45], and comparing the pre- and postcoalescence instants, we observe very good agreement between the numerical and experimental results demonstrating the predictive capability of our numerical model. Due to the experimental limitations, the data comparison is reported only for $-1.6 \leq z \leq 1.6$ where $z = 0$ refers to the symmetry plane. It is remarkable to observe that the numerical technique we use captures the whole closure and plug-formation process, handling the topological change leading to the liquid plug formation. This aspect constitutes the limitations of lubrication approaches, which were capable of modeling the closure up to $R_{\min} = \min(R_1) = 0.4$, or sharp-interface methods such as the one employed by Tai *et al.* [38], which were able only to extend the limit to $R_{\min} = 0.1$. We anticipate that a reliable computation of the phases after closure will provide important insights of the physics of the phenomenon and will demonstrate the physiological relevance of injuries due to airway closure. However, it is beyond the scope of this paper to investigate the formation of the liquid plug in the very proximity of the coalescence event. The main focus of our investigation is on the pre- and postcoalescence phase for $|t - t_c| > 0.01t_c$. A further proof that our numerical approach is well suited to our study is provided in Sec. IV C, where the asymptotic power law predicted in Ref. [38] as $R_{\min} \propto (t_c - t)^\gamma$ is confirmed by our numerical results.

An additional validation is provided in Fig. 4, where the flow velocity fields and the streamlines in the glycerol-oil system are reported. The numerical predictions compare very well, qualitatively and quantitatively, with the experimental measurements obtained by micro-PIV. Four instantaneous conditions are experimentally available, for which velocity vectors and streamlines are reported in Ref. [37], two for the precoalescence [Figs. 4(a) and 4(b)] and two for the postcoalescence [Figs. 4(e) and 4(f)] phase. Corresponding numerical results are depicted in Figs. 4(c) and 4(d) and 4(g) and 4(h). The same scale for the color bar is employed in all the cases to facilitate a direct comparison. Before coalescence, the pressure gradient induced by a capillary instability drains the fluid from the thin film near the pipe wall to the bulge [see, e.g., green arrows in Fig. 4(c)] driving the coated liquid layer to closure. The maximum velocity is located at the bulge tip, and it is directed in radial direction. Another local maximum of the velocity magnitude is observed in the thin film right at the connection between the thin film and the bulge, where the liquid draining produces a strong axial velocity towards the bulge. A strong radial acceleration is observed between the first two snapshots. The radially dominated flow field precoalescence turns into an axially dominated flow field postcoalescence, when the core fluid is pinched off by the annular liquid bulge and the plug is formed. The largest velocities are observed after the coalescence and further drain the liquid film

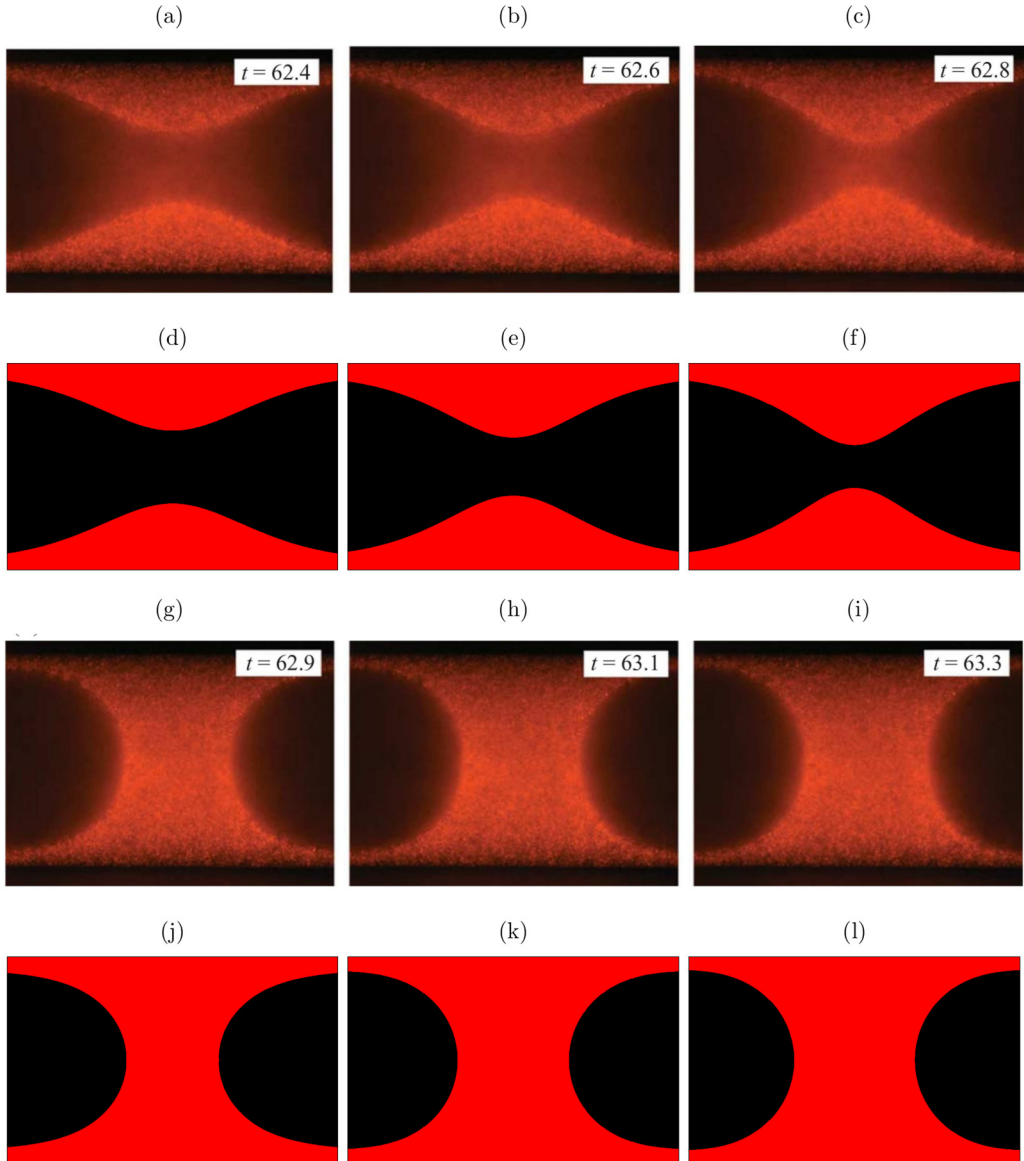


FIG. 3. Comparison of the two-phase distribution at different times: first (a)–(c) and third (g)–(i) rows from the top are the experimental visualizations reported in Ref. [37] using fluorescent particles, whereas second (d)–(f) and fourth (j)–(l) rows from the top are our numerical results for the corresponding time relative to the coalescence event. The annular film is in red, while the core fluid is in black. The nondimensional parameters of interest are $\varepsilon = 0.23$, $La = 0.072$, $\mu = 0.01$, $Q = 0.95$, and $\lambda = 9.2$ and the closure event is depicted in the axial range $-1.6 \leq z \leq 1.6$. Time is scaled as in Ref. [37] by $\mu_L a / \varepsilon^3 \sigma$. (a)–(f) The pre-coalescence phase due to the interfacial instability; (g)–(l) the post-coalescence phase, where a bifrontal plug growth is observed.

lining the pipe wall to supply the newly formed plug with additional liquid. At the same time the plug advances axially, in a symmetric fashion, compressing the two-fluid interface and leading to formation of a capillary wave, which is responsible for high stress levels along the pipe wall as will be discussed in detail later. This process is here addressed as *bifrontal plug growth*.

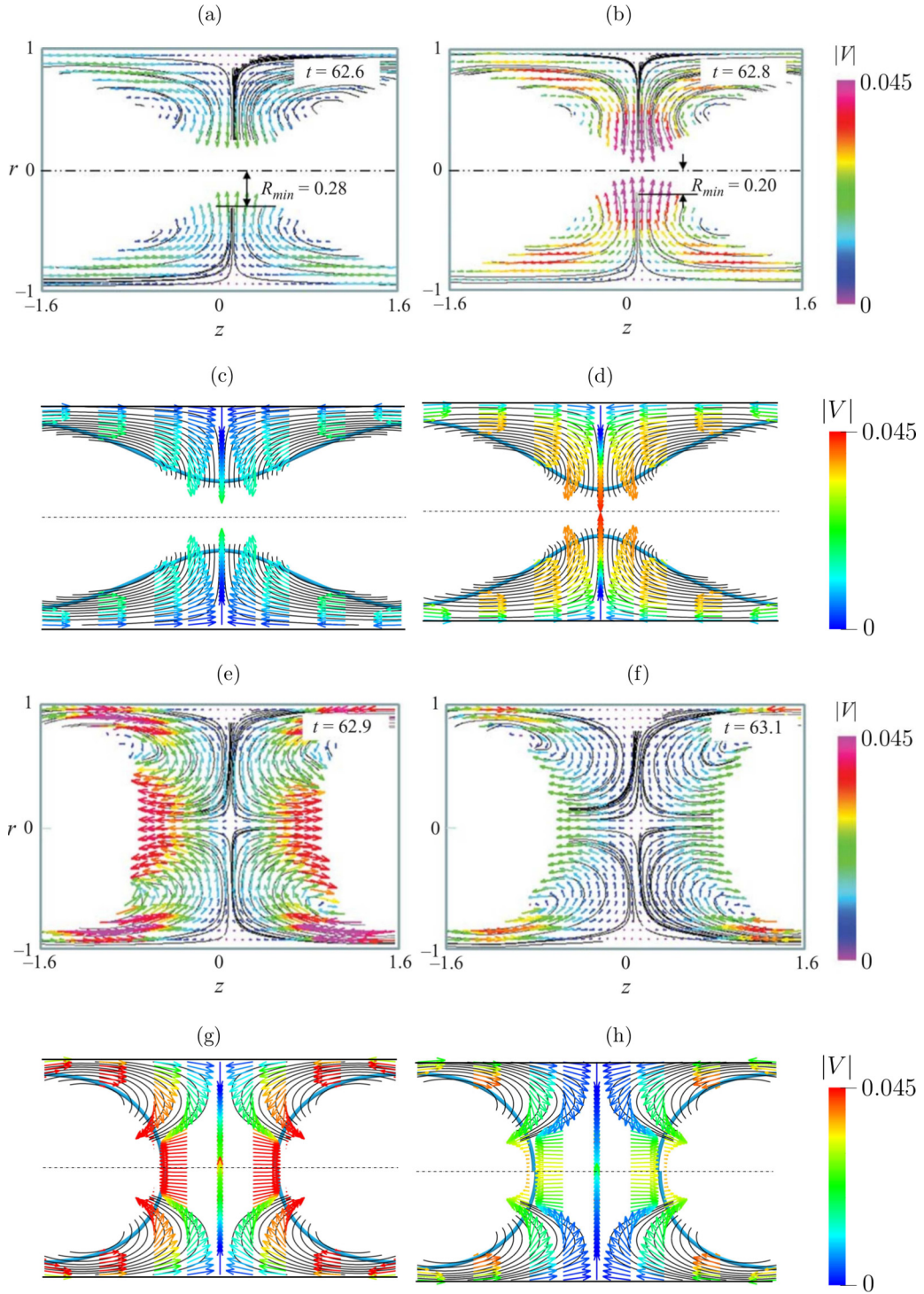


FIG. 4. Velocity vectors (arrows) and streamlines for $\varepsilon = 0.23$, $La = 0.072$, $\mu = 0.01$, $\varrho = 0.95$, and $\lambda = 9.2$: first (a)–(b) and third (e)–(f) rows from the top are the micro-PIV measurements of Ref. [37], whereas second (c)–(d) and fourth (g)–(h) rows from the top are numerical results. Time is scaled by $\mu_L a / \varepsilon^3 \sigma$.

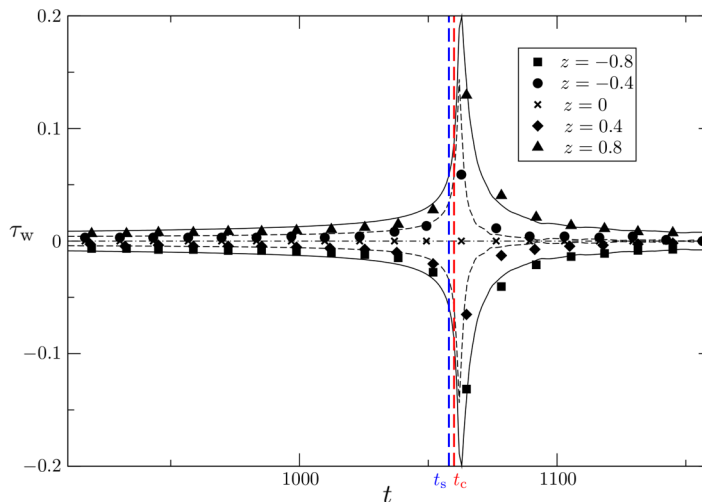


FIG. 5. Temporal evolution of the wall shear stress between $-0.8 \leq z \leq 0.8$: the solid black lines denote the numerical results for $z = \pm 0.8$, the dashed black lines for $z = \pm 0.4$, while the dashed-dotted line refers to $z = 0$; markers refer to the experimental results of Ref. [37] as indicated in the legend. The two colored dashed lines denote the closure time (t_c) and the numerical limit (t_s) of Ref. [38]. In these results the numerical closing time t_c is used as the reference time, and the experimental results are thus shifted in time to match with it, considering the scaling employed in (2).

The last comparison between experiments and numerics is dedicated to the shear stress along the pipe wall, $\tau_w = -\tilde{\mu} \partial_r u_z|_{r=1}$, where, for the current scaling, $\tilde{\mu} = 1$ in the coating fluid. Figure 5 depicts the comparison between our simulations (lines) and the experimental measurements (markers) at five axial locations along the wall between $-0.8 \leq z \leq 0.8$. As seen, the numerical results are in good quantitative agreement with the experimental data, which completes the validation of our numerical model.

Beside the demonstrated accuracy of our simulations, it is important to stress the peculiar feature of the wall shear stress during the closure process. As can be seen from Fig. 5, the rapid growth of the shear stress in time, which is associated with the capillary instability, does not experience a maximum at the closure time, but keeps growing even after coalescence, and reaches the maximum value at $t = t_m > t_c$ and then relaxes toward the final equilibrium value. The bifrontal plug growth actually appears to be the most relevant and critical phase for the wall shear stresses regarding the epithelial cell damage. This feature can be inferred also by the experimental measurements and further implies the importance for numerical simulations to be able to handle a topological change of the liquid film. It is emphasized here that the previous computational predictions were restricted up to an instant before the closure ($t \leq t_s$) and thus missed the most important phase of the physiological significance and could only conservatively estimate the maximum shear stress at the walls. Moreover, even though the coalescence process was well captured by the experimental measurements, the limited time resolution prevented the experimental measurements to capture the sharpest peak of τ_w , which is well resolved by the numerical simulations as shown in Fig. 5. As a result, the experiments also tend to underestimate the maximum wall shear stress and the stress-induced cell damage, as well as all the quantities which experience a very sharp growth. In this case, the maximum shear stress measured in the experiments is 25% smaller than the numerical peak.

B. Airway closure: Relevant lung airway parameters

After the validation of the numerical method, simulations are performed to examine the airway closure in the physiological conditions. The radius of an adult lung airway at tenth generation is

TABLE II. Summary of the 18 cases simulated, with the corresponding nondimensional groups.

λ	ϱ	μ	La	ε
6	10^{-3}	1.5×10^{-3}	100	0.2, 0.25, 0.3
			200	
		3×10^{-4}	4	
			8	
		1.5×10^{-4}	1	
			2	

approximately $a = 0.065$ cm (see, e.g., Ref. [48]), and typical length-to-diameter ratios for an airway are of the order of 3, i.e., $\lambda = 6$. Aiming at modeling airway closure in the ninth to tenth branching generation, these parameters will be assumed throughout our study. We stress that it is physiologically relevant to define the parameter range in terms of the dimensional quantities (i.e., ρ_L , ρ_G , μ_L , μ_G , σ , R and L) and then derive the corresponding nondimensional groups. In particular, varying μ_L , in fact, makes physiological sense since a change of mucus viscosity can be due to a pathology or to aging, and it has an impact on both the Laplace number (La) and the liquid-to-gas viscosity ratio (μ), whereas varying μ and keeping La constant does not have any physiological correspondence.

Following Tai *et al.* [38], we additionally assume that the lining liquid can be modeled as a Newtonian fluid with the properties resulting from a mixture between mucus and serous layers. The density of the two fluids is not far from that of water, and excursions in ρ_L are normally negligible. The density ratio between air and water at 37 °C is $\varrho = 1.14 \times 10^{-3}$, so $\varrho = 10^{-3}$ is representative of the gas-to-liquid density ratio characterizing the mucus-serous mixture in the liquid film and the core fluid made out of air. Therefore, $\varrho = 10^{-3}$ is employed in all the simulations presented in this paper. Proceeding with our conceptual homogenization adopted to deal with the mixture of mucus and serous layer, we must consider that the liquid film is more viscous than water. Following Ref. [38], we assume that $\mu_L = 0.13$ poise and take the dynamic viscosity of air at 37 °C as $\mu_G = 1.89 \times 10^{-4}$ poise, which yields the gas-to-liquid dynamic viscosity ratio of $\mu = 1.45 \times 10^{-3}$. The serous layer is very watery ($\mu_S \approx \mu_H = 0.01$ poise, where the subscripts S and H denote serous liquid and water, respectively) and the dynamic viscosity of mucus (see e.g., Ref. [49]) is reported to range over several orders of magnitude, passing from 10 to 10 000 times the reference value for water depending on age, physiological function, and eventual pathological conditions (i.e., $10\mu_H \leq \mu_M \leq 10\,000\mu_H$, which corresponds to 0.1 poise $\leq \mu_M \leq 100$ poise, where M refers to mucus). Hence, the dynamic viscosity ratio (and the Laplace number) is varied in our study taking μ_L in the range $0.126 \leq \mu_L \leq 1.26$, which yields to $1.5 \times 10^{-4} \leq \mu \leq 1.5 \times 10^{-3}$.

The last assumption in our airway closure model is related to the surface tension σ between the liquid film and the air core fluid. During the normal operating conditions, the surfactants released in the lungs tend to decrease the interfacial surface tension to values much lower than the surface tension $\sigma_H = 70$ dyn cm⁻¹ at the clean water-air interface, penalizing the Plateau-Rayleigh instability. Hereinafter we assume that the surface tension is constant, and the value $\sigma = 26$ dyn cm⁻¹ is chosen to represent normal conditions, whereas $\sigma = 52$ dyn cm⁻¹ is used to mimicking surfactant-deficient pathological conditions, which are typically associated to the airway closure phenomenon. This leads to $1 \leq \text{La} \leq 200$. Therefore, simulations are performed for a total of six combinations of μ and La values, as summarized in Table II, together with the three initial film thicknesses, i.e., $\varepsilon = 0.2, 0.25, \text{ and } 0.3$.

C. Analysis of a typical airway closure scenario

A typical scenario observed during an airway closure is depicted in Fig. 6 characterizing the coalescence process for $\text{La} = 200$, $\mu = 1.5 \times 10^{-3}$, $\varrho = 10^{-3}$, $\lambda = 6$, $\varepsilon = 0.25$ in terms of pressure

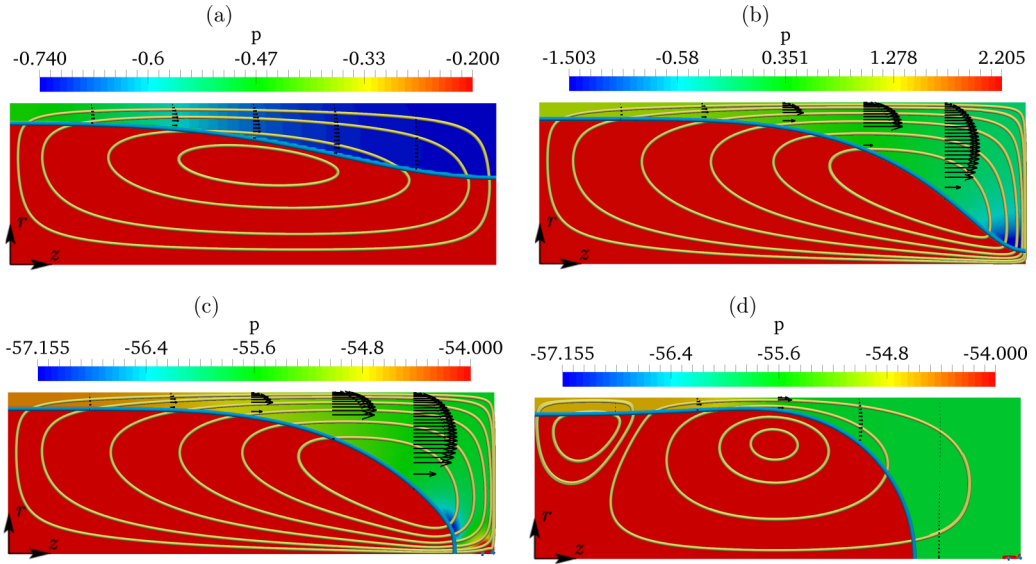


FIG. 6. Pressure field (colors), streamlines (yellow lines) and axial velocity in the liquid phase (arrows) at two pre-coalescence [(a) $t = 600$ and (b) $t = 736$] and two post-coalescence instants [(c) $t = 737$ and (d) $t = 800$]. The turquoise line denotes the interface location. The phenomenon is symmetric in z .

field (color field), streamlines (yellow lines), interface location (turquoise line), and axial velocity in the liquid (arrows). In the initial growth phase of the instability, the cross-sectional curvature of the interface $1/R_I$ expands the flow in the liquid film at the location where the bulge is. This curvature effect dominates over the in-plane compression due to a thicker liquid film at the bulge, and the lowest relative pressure is observed at the axial location of the bulge tip [see Fig. 6(a)]. Since the selected initial thickness of the film is greater than the critical thickness $\epsilon = 0.12$, the airway closure occurs within a breathing cycle. As observed in the previous subsection, this capillary instability drains the liquid from the film (see arrows) to supply the bulge up to the liquid plug formation.

Compared to the early stage in Fig. 6(a), the snapshot taken just prior to coalescence [Fig. 6(b)] exhibits a qualitative difference in the pressure profile, i.e., the pressure has a minimum at the bulge tip with a sharp gradient in the radial direction. The increase of maximum shear stress in this phase is evidently seen in the velocity field (arrows) as the radial derivative of u_z experiences a significant increase between $t = 600$ [Fig. 6(a)] and $t = 736$ [Fig. 6(b)]. Consistent with the predictions of Ref. [38], the streamlines (yellow lines) become more and more elongated in the radial direction as the perturbation grows. After the coalescence [see Fig. 6(c)], the pressure field has its minimum at the liquid-gas interface near the centerline of the tube (blue area). The flow is then pushed away from the plane of symmetry and drains even more liquid from the thin coating film to form the liquid plug closing the airway. This phase corresponds to the formation of a liquid plug in which the air-liquid interface advances with its two fronts in opposite directions (bifrontal plug growth; see, e.g., Ref. [50]). The process occurs in a very short time and is characterized by high axial accelerations. Such a quick post-coalescence phase is comparable to the receding of two air fingers, whose fronts are moving in opposite directions. We anticipate that during closure and also shortly afterwards, the pressure and the shear stress experience a sharp increase which is comparable to the one observed during propagation of liquid plugs and receding of air fingers. Few instants after closure, the stresses relax in magnitude down to a stationary state [almost reached at $t = 800$; see Fig. 6(d)], which is achieved when the plug stops growing and the pressure field is solely determined by the equilibrium Laplace pressure across the interface.

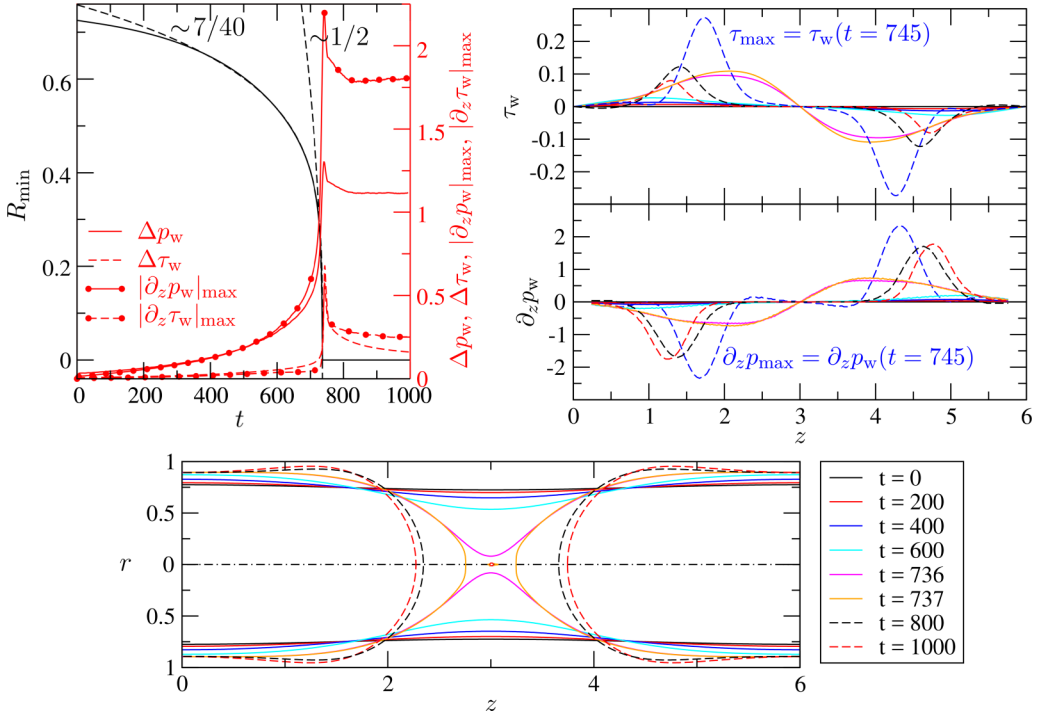


FIG. 7. Bottom panel: Location of the liquid-gas interface at significant instants in time. Top-right panel: wall shear stress τ_w and wall pressure gradient $\partial_z p_w$ depicted with the same color coding of the time legend. Top-left panel: minimum of the interface radial location $R_{\min} = \min(R_I)$ (solid black line), asymptotic power laws predicted in Ref. [38] (dashed black line), excursions of wall pressure $\Delta p_w = \max(p_w) - \min(p_w)$ and shear stress $\Delta \tau_w = \max(\tau_w) - \min(\tau_w)$ depicted as solid and dashed lines without markers, maximum absolute values of wall pressure and wall shear stress gradients, $|\partial_z p_w|_{\max}$ and $|\partial_z \tau_w|_{\max}$, respectively, depicted by solid and dashed red lines marked with bullets. The nondimensional groups are $\text{La} = 200$, $\mu = 1.5 \times 10^{-3}$, $\varrho = 10^{-3}$, $\lambda = 6$, and $\varepsilon = 0.25$.

One of the main focuses of our study is to determine the mechanical stress level on the pipe wall and, consequently, on the epithelial cells. Figure 7 correlates these quantities with the time evolution of the liquid-gas interface shown in the bottom panel. The minimum of the interface radial location R_I is depicted as a solid black line in the top-left panel, and it is used to accurately identify the closure event and correlate it with the stresses and their gradients at the pipe wall (red lines). The dashed black lines denote the power-law fits $R_{\min} \propto (t_c - t)^{1/2}$ and $R_{\min} \propto (t_c - t)^{7/40}$, which are valid near and far from the coalescence time t_c , respectively [38], confirming the expected asymptotic behavior. These same asymptotic trends hold true throughout the parameter space considered in our study; moreover, also the stress excursions seem to follow the 7/40-power law far from the coalescence event. According to Refs. [51,52], severe injuries for the epithelial cells are caused by the presence of high-pressure gradients, a high level of shear stress and of shear stress gradient at the airway walls. For these reasons, in Fig. 7 (top-left panel) the excursions of wall pressure $\Delta p_w = \max(p_w) - \min(p_w)$ and shear stress $\Delta \tau_w = \max(\tau_w) - \min(\tau_w)$ are depicted together with the maximum absolute values of wall pressure and shear stress gradients denoted by $|\partial_z p_w|_{\max}$ and $|\partial_z \tau_w|_{\max}$, respectively. The axial distribution of wall shear stress and wall pressure gradient are also plotted in the top-right panel of Fig. 7 to show the areas which are more dangerous for the epithelial cells.

It is noteworthy to observe that the very sharp peaks in all the relevant wall stress quantities are correlated with the bifrontal plug growth. To the best of our knowledge, this feature of airway

closure has been overlooked, so far, in all the previous investigations, which focused on only the plug rupture process for addressing the epithelial cell damage in human lungs. Here we demonstrate that the shear stress may reach $\max_{t,z}(|\tau_w|) \approx 0.28$ just after the coalescence, which, in dimensional quantities, corresponds to 224 dyn cm^{-2} , almost three times larger than the estimate in Ref. [38], which stopped the simulations right before the coalescence. Very similar trends are also observed for the pressure excursion Δp_w , which provides a good estimate of the average normal stress gradient over the pipe wall when it is divided by the pipe aspect ratio λ . As depicted in Fig. 7, Δp_w has a peak value of $\max_t(\Delta p_w) \approx 1.3$, which corresponds to the dimensional value 1040 dyn cm^{-2} , with an average maximum wall pressure gradient of $\max_t(\Delta p_w)/\lambda \approx 0.216$, i.e., $2.6 \times 10^3 \text{ dyn cm}^{-3}$. The estimate becomes much more dramatic for cells injury if we consider the maximum local pressure gradient $\max_{t,z}(|\partial_z p_w|) \approx 2.2$, which corresponds to $2.7 \times 10^4 \text{ dyn cm}^{-3}$ [a factor 10 bigger than $\max_t(\Delta p_w)/\lambda$]. Very severe wall shear stress gradients are also seen in Fig. 7, where $\max_{t,z}(|\partial_z \tau_w|) \approx 0.65$, i.e., $8 \times 10^3 \text{ dyn cm}^{-3}$. As mentioned in the previous remarks, the highest peaks of damaging stress levels for the epithelial cells occur during the postcoalescence phase, and an estimate of them using the precoalescence measurements can only be very conservative. This is well depicted in the top-left panel of Fig. 7. As seen, $|\partial_z p_w|_{\max}$ and Δp_w at closure are at about half of their peak values, and $|\partial_z \tau_w|_{\max}$ and $\Delta \tau_w$ do not even make it to one third of their peak values during the precoalescence phase including the closure time.

An interesting qualitative feature characterizing the wall stresses during the closure process is the change of shape of the distributions of the pre- and postcoalescence stresses and their gradients. Tai *et al.* [38] noticed a certain self-similarity between the shear stresses prior to the closure: This self-similarity is lost after closure and the smooth s-shape function which well fits τ_w and $\partial_z p_w$ before the coalescence turns into a two-hump function with a point symmetry (see Fig. 7, top-right panel).

A fine detail of the interface dynamics is that a satellite bubble is trapped inside the liquid plug, as previously reported by Ref. [31]. A varicose fluid thread is observed before plug coalescence (not shown). The major differences with the results of Ref. [31] is the thread in our study is very short in longitudinal length. This quantitative difference is mainly caused by the viscosity ratio $\tilde{\mu} = 1$ employed in Ref. [31], which strongly differs from $\tilde{\mu} \in [1.5 \times 10^{-4}, 1.5 \times 10^{-3}]$ used in ours. For a detailed analysis about the viscous-blocking mechanism in liquid lined pipes, we refer the reader to Ref. [32].

The last remark is related to the location of the two humps in $\partial_z p_w$ and τ_w after the closure. Their maximum absolute values are located at the minimum film thickness along the pipe wall, which recedes from the symmetry plane following the motion in the liquid menisci, compressed by the plug formation.

D. Effect of surface tension σ

The Laplace number is linearly proportional to the surface tension. Thus simulations are performed for $La = 200$ and $La = 100$ to investigate the effects of the surface tension while keeping the other parameters constant at $\mu = 1.5 \times 10^{-3}$, $\rho = 10^{-3}$, $\lambda = 6$, and $\varepsilon = 0.25$. Qualitatively, the evolution of the interface and the distribution of the wall pressure gradient and of the wall shear stress for $La = 100$ are very similar to the results plotted for $La = 200$ in Fig. 7. Hence, the results for $La = 100$ are not depicted hereinafter.

Considering the creeping-flow limit, i.e., $La \rightarrow 0$, the convective terms in the momentum equation are negligible, and the solution of the nondimensional mathematical model depends only on \tilde{q} , $\tilde{\mu}$, ε , and λ . Hence, after selecting the two fluids and fixing the geometry and the initial film thickness, the solution of the Stokesian flow is unique. This implies that, with the current capillary scaling, the nondimensional closure time is independent of σ , and therefore the dimensional closure time is inversely proportional to σ : i.e., doubling σ halves $t_c \mu_L a / \sigma$. Figure 8 depicts R_{\min} , the wall stresses, and their gradients against time for $La = 100$. The closure event, quantified by means of R_{\min} , is slightly delayed, in nondimensional time units, by increasing the surface tension σ . Indeed,

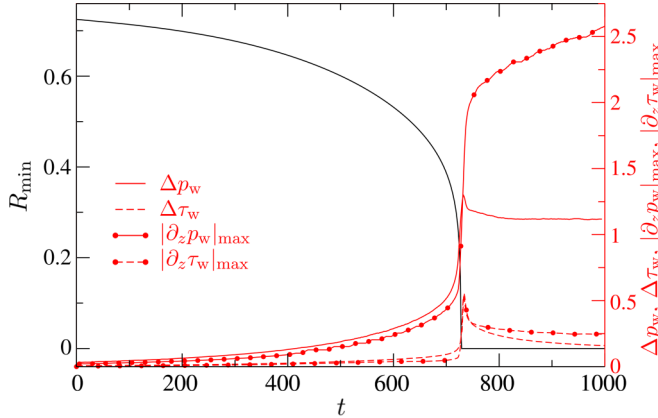


FIG. 8. Minimum of the interface radial location $R_{\min} = \min(R_I)$ (solid black line), excursions of wall pressure $\Delta p_w = \max(p_w) - \min(p_w)$ and shear stress $\Delta \tau_w = \max(\tau_w) - \min(\tau_w)$ depicted as solid and dashed lines without markers, and maximum absolute values of wall pressure and wall shear stress gradients, $|\partial_z p_w|_{\max}$ and $|\partial_z \tau_w|_{\max}$, respectively, depicted by solid and dashed red lines marked with bullets. The nondimensional groups are $La = 100$, $\mu = 1.5 \times 10^{-3}$, $\rho = 10^{-3}$, $\lambda = 6$, and $\varepsilon = 0.25$.

for $La = 200$ the airway closure occurs between $t = 736$ and $t = 737$, whereas for $La = 100$ the minimum radial coordinate of the interface reaches zero between $t = 727$ and $t = 728$. The longer nondimensional closure time t_c produced by an increase of σ is due to an increased inertia which the flow acquire upon an increase of La . We anticipate that this effect is, however, negligible when it is compared to the sensitivity of t_c to the perturbation amplitude (see Ref. [38]) or to the initial film thickness ε , as discussed in the following subsections. The increasing inertia due to a higher Laplace number only delays the nondimensional closure time t_c . Still, increasing σ decreases the dimensional closure time $t_c \mu_L a / \sigma$. In fact, $736 \leq t_c \leq 737$ obtained for $\sigma = 52 \text{ dyn cm}^{-1}$, i.e., $La = 200$, corresponds to a dimensional closure time $t_c \mu_L a / \sigma \approx 0.116 \text{ s}$, whereas $727 \leq t_c \leq 728$, referred to $La = 100$ and $\sigma = 26 \text{ dyn cm}^{-1}$, corresponds to $t_c \mu_L a / \sigma \approx 0.229 \text{ s}$. This consideration makes clear the subtle counterintuitive closure delay (in nondimensional time units only) due to an increase of La ; i.e., the delay is induced by the fact that σ is used in scaling t .

Extending this analysis to the stress-related quantities, the peak values observed for Δp_w , $\Delta \tau_w$ and $|\partial_z \tau_w|_{\max}$ are quantitatively very similar: As the Laplace number decreases from $La = 200$ to $La = 100$, the peak values of Δp_w , $\Delta \tau_w$, and $|\partial_z \tau_w|_{\max}$ decrease about 0.5%, 5%, and 20%, respectively. In addition, this weak dependence of Δp_w , $\Delta \tau_w$, and $|\partial_z \tau_w|_{\max}$ translates into a nearly linear growth of their corresponding dimensional values with the surface tension, for instance, if $\max_{t,z}(|\tau_w|) \approx 0.28$ for $La = 200$ (and $\sigma = 52 \text{ dyn cm}^{-1}$) corresponds to 224 dyn cm^{-2} , $\max_{t,z}(|\tau_w|) \approx 0.27$ for $La = 100$ (and $\sigma = 26 \text{ dyn cm}^{-1}$) corresponds to 108 dyn cm^{-2} . This same trend is also observed in all other cases investigated in this study (see Table III).

The main qualitative and quantitative difference between $La = 100$ and $La = 200$ is seen in the time evolution of the maximum absolute value of the wall pressure gradient. For $La = 200$ a pronounced peak is observed (see Fig. 7). This is correlated to the airway closure and quickly fades out from $|\partial_z p_w|_{\max} \approx 2.2$ to $|\partial_z p_w|_{\max} \approx 1.8$ for then experiencing a relatively slow increase. As shown in Fig. 7, the bifrontal plug growth induces the propagation of a capillary wave. For $La = 100$, the stresses due to the capillary wave overshadow the spikelike contribution induced by the plug formation, and the compression of the liquid menisci induces a rapid increase in $|\partial_z p_w|_{\max}$ during the plug formation and the maximum pressure gradient keeps growing monotonically in time during the postcoalescence phase, but with a much slower rate (see Fig. 8). As a result, decreasing the Laplace number brings to a higher postcoalescence $|\partial_z p_w|_{\max}$, by more than 35%. The monotonically growing trend of $|\partial_z p_w|_{\max}$ is discussed in more detail in Sec. IV G.

TABLE III. Summary of the closure time, the maximum wall stress excursions and the maximum tangential wall stress gradients for all the 18 cases simulated in our study.

μ	La	ε	t_c	$\max_t(\Delta p_w)$	$\max_t(\Delta \tau_w)$	$\max_t(\partial_z \tau_w _{\max})$
1.5×10^{-3}	100	0.2	2831	1.369	0.495	0.637
		0.25	727	1.297	0.534	0.551
		0.3	265	1.339	0.572	0.538
	200	0.2	2839	1.357	0.525	0.773
		0.25	737	1.303	0.571	0.678
		0.3	275	1.341	0.607	0.648
3×10^{-4}	4	0.2	2215	1.404	0.385	0.392
		0.25	617	1.441	0.425	0.424
		0.3	227	1.455	0.426	0.464
	8	0.2	2215	1.411	0.380	0.393
		0.25	616	1.418	0.438	0.423
		0.3	228	1.432	0.408	0.468
1.5×10^{-4}	1	0.2	2209	1.371	0.378	0.392
		0.25	615	1.449	0.420	0.452
		0.3	226	1.471	0.463	0.478
	2	0.2	2211	1.297	0.380	0.392
		0.25	736	1.347	0.570	0.679
		0.3	227	1.463	0.461	0.466

E. Effect of liquid film dynamic viscosity μ_L

The dynamic viscosity of the liquid phase has a twofold effect on the nondimensional groups: (1) it affects the Laplace number in a quadratically inverse manner, i.e., $La \propto \mu_L^{-2}$ and (2) it is inversely proportional to the gas-to-liquid dynamic viscosity ratio, i.e., $\mu \propto \mu_L^{-1}$.

Increasing the liquid dynamic viscosity, for instance, upon an increase of the mucus viscosity, decreases the Laplace number and the relative importance of viscous forces exerted by the air core flow on the liquid film, slowing down the airway closure in dimensional time. This phenomenon is demonstrated in Fig. 9, where the parameters $\varrho = 10^{-3}$, $\lambda = 6$, and $\varepsilon = 0.25$ are kept constant

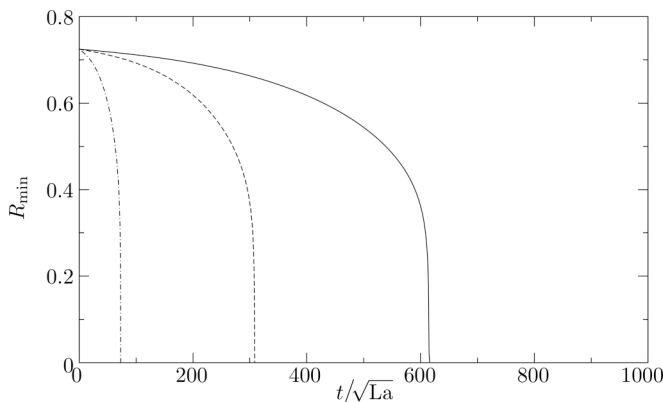


FIG. 9. The effects of the liquid viscosity. The time evolution of the minimum radius of the interface, R_{\min} , is plotted for $\varrho = 10^{-3}$, $\lambda = 6$, $\varepsilon = 0.25$, and $La = 1$, and $\mu = 1.5 \times 10^{-4}$ (solid line), $La = 4$, and $\mu = 3 \times 10^{-4}$ (dashed line), $La = 100$, and $\mu = 1.5 \times 10^{-3}$ (dashed-dotted line).

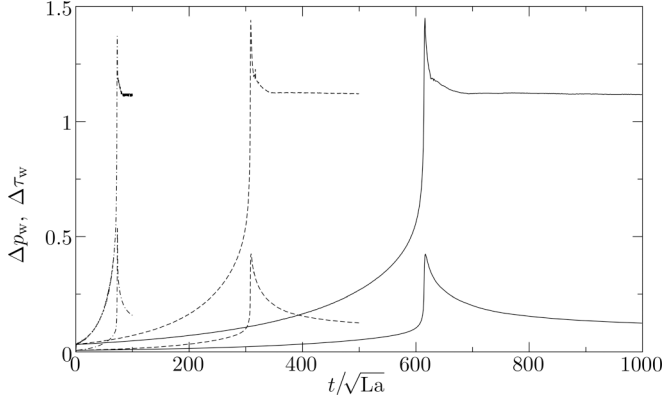


FIG. 10. The effects of the liquid viscosity on the time evolution of the excursion of wall stresses Δp_w (higher-amplitude curves) and $\Delta \tau_w$ (lower-amplitude curves) for $\varrho = 10^{-3}$, $\lambda = 6$, $\varepsilon = 0.25$ and $La = 1$, $\mu = 1.5 \times 10^{-4}$ (solid line), $La = 4$ and $\mu = 3 \times 10^{-4}$ (dashed line), $La = 100$ and $\mu = 1.5 \times 10^{-3}$ (dashed-dotted line).

and three combinations of La and μ are considered: $La = 1$, $\mu = 1.5 \times 10^{-4}$ (solid line), $La = 4$, $\mu = 3 \times 10^{-4}$ (dashed line), $La = 100$, $\mu = 1.5 \times 10^{-3}$ (dashed-dotted line), which correspond to $\mu_L = 0.126$, 0.252 , and 1.26 poise in our airway closure model, respectively. The reduction of flow inertia and relative viscous resistance of air have a dramatic impact on R_{\min} , especially due to the Laplace number, which increases by two orders of magnitude if μ_L decreases by one order. For removing the dynamic viscosity of the liquid from the time axis, the nondimensional time is scaled as t/\sqrt{La} in Fig. 9. In dimensional quantities, upon an increase of μ_L , the dimensional closure time increases from $t_c = 0.229$ s for $\mu_L = 0.126$ poise to $t_c = 1.934$ s for $\mu_L = 1.26$ poise. As a result, increasing the dynamic viscosity of the liquid phase slows down the airway closure process, as also reported for the Stokes-flow limit in Refs. [31,53].

The effect of the liquid film dynamic viscosity on the excursion of wall stresses is shown in Fig. 10. As seen, a decrease of μ_L tends to decrease the excursion in normal stress Δp_w and to increase and sharpen the one in shear stress $\Delta \tau_w$ at the wall. The same trend is observed for $|\partial_z p_w|_{\max}$ and $|\partial_z \tau_w|_{\max}$, which slightly grow upon a decrease of μ_L (not shown).

The wiggles observed in the results are of numerical origin. They are due to the very quick dynamics of the pre- and postcoalescence phases, to the presence of a pressure jump across the interface, and to the challenging viscosity ratios tackled in this study. Analogous computational features are also reported by other numerical studies when similar flow configurations are considered; see e.g., Refs. [54,55].

F. Effect of the film thickness ε

The initial thickness of the liquid film has a major impact on the airway closure time. This has been demonstrated by Refs. [37,38] in previous investigations and is confirmed here for $\varepsilon = 0.2$, 0.25 , and 0.3 , as shown in Fig. 11 (black lines). Our main focus is, however, on the effects of ε on the stress level at the airway wall.

Figure 11 reports (in red lines) the excursions of wall pressure Δp_w and shear stress $\Delta \tau_w$ as well as the maximum absolute values of wall pressure and shear stress gradients, $|\partial_z p_w|_{\max}$ and $|\partial_z \tau_w|_{\max}$, as a function of time for three initial film thicknesses: $\varepsilon = 0.2$, 0.25 , and 0.3 . The other parameters are kept constant at $La = 1$, $\mu = 1.5 \times 10^{-3}$, $\varrho = 10^{-3}$, and $\lambda = 6$.

The peak value and the trend of Δp_w , $\Delta \tau_w$, and $|\partial_z \tau_w|_{\max}$ remain almost unchanged when the film thickness changes; however, the maximum absolute value of the wall pressure gradient $|\partial_z p_w|_{\max}$ experiences a remarkable increase when the initial film thickness ε decreases. This is observed in

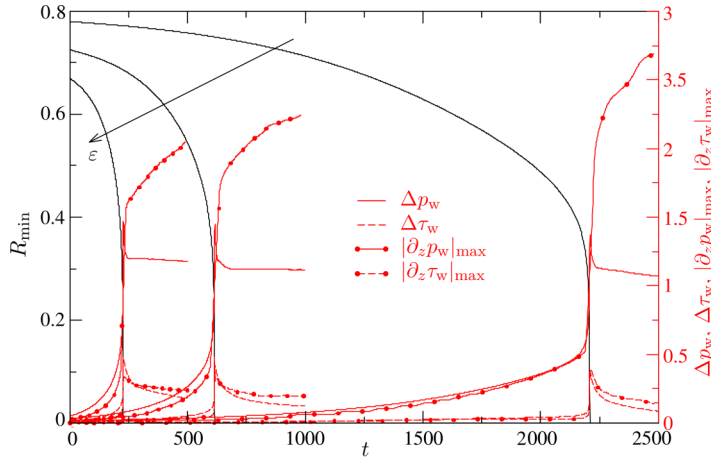


FIG. 11. The effects of the initial liquid film thickness on the minimum radius of the interface R_{\min} (solid black line) and excursions of wall pressure $\Delta p = \max(p_w) - \min(p_w)$ and shear stress $\Delta \tau = \max(\tau_w) - \min(\tau_w)$ depicted as solid and dashed lines without markers, and the maximum absolute values of wall pressure and shear stress gradients, $|\partial_z p_w|_{\max}$ and $|\partial_z \tau_w|_{\max}$, respectively, depicted by solid and dashed red lines marked with bullets. The nondimensional groups in common are $La = 1$, $\mu = 1.5 \times 10^{-3}$, $\varrho = 10^{-3}$, and $\lambda = 6$; the three sets of curves refer to $\varepsilon = 0.2, 0.25, \text{ and } 0.3$.

all our simulations. The wall pressure gradient $|\partial_z p_w|_{\max}$ is related to the local variation of film thickness, which is produced by the compression of the liquid menisci due to the bifrontal plug growth. A lower initial film thickness ε produces thinner menisci right beyond the plug, which explains why $|\partial_z p_w|_{\max}$ increases when ε decreases.

G. Effect of the postcoalescence dynamics on the wall pressure gradient

Figure 8 has shown that the maximum wall pressure gradient $|\partial_z p_w|_{\max}$ can experience a monotonically growing trend in time, qualitatively different from the one reported in Fig. 7. The formation of the liquid plug, its bifrontal growth, the consequent compression of the liquid film on the pipe wall, and the propagation of the capillary wave are responsible for this effect. Figure 12 depicts the time evolution of minimum radial (R_{\min} , black solid line) and axial coordinate of the interface (Z_{\min} , black solid line with bullets), the minimum film thickness [$1 - \max(R_I)$, turquoise solid line] and its axial location for $z < 3$ (Z_{mt} , turquoise solid line with bullets), and the maximum wall pressure gradient for $La = 1$, $\mu = 1.5 \times 10^{-3}$, $\varrho = 10^{-3}$, $\lambda = 6$, and $\varepsilon = 0.25$. After the closure event, the bifrontal plug growth, shown by the growing trend of Z_{\min} , forms a capillary wave on the shoulder of each of the two interface fronts. These waves compress the liquid film against the airway wall [see $1 - \max(R_I)$] and slowly propagate symmetrically in axial direction (see the negative trend of Z_{mt} in the postcoalescence phase). The correlation between the monotonic growing trend of $|\partial_z p_w|_{\max}$, the liquid plug, and the thin film dynamics is evident from Fig. 12.

H. Comparison of maximum wall stresses and closure times

The maximum of the wall stress excursions $\max_t(\Delta p_w)$ and $\max_t(\Delta \tau_w)$ and the maximum wall shear stress gradient $\max_t(|\partial_z \tau_w|_{\max})$ are reported in Table III, together with the closure time t_c for all the parameters investigated in this study. The qualitative trends reported in the previous sections for the wall stresses and their gradients are found to persist in all the simulations. The nondimensional closure time is remarkably affected by the initial film thickness and experiences significant variations upon a change of μ_L . The maximum of the wall pressure excursion is almost insensitive

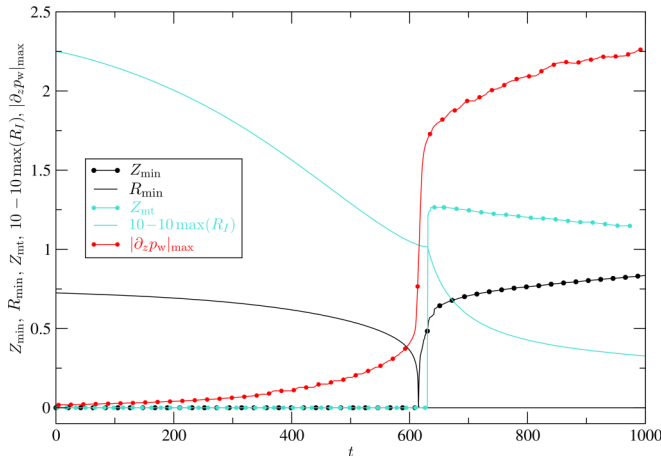


FIG. 12. The time evolutions of the minimum radius of the interface, R_{\min} (black line), the minimum axial distance between the fronts, Z_{\min} (black line with bullets), the minimum film thickness, $1 - \max(R_f)$ (turquoise solid line), its axial location for $z < 3$, Z_{mt} (turquoise solid line with bullets), and the maximum wall pressure gradient $|\partial_z p_w|_{\max}$. The nondimensional groups are $La = 1$, $\mu = 1.5 \times 10^{-3}$, $\varrho = 10^{-3}$, $\lambda = 6$, and $\varepsilon = 0.25$.

to all the parameters investigated in this study, being always within $1.3 \leq \max_t(\Delta p_w) \leq 1.48$. A more relevant effect of ε , μ_L , and σ is reported in Table III for $\max_t(\Delta \tau_w)$ and $\max_t(|\partial_z \tau_w|_{\max})$, which are characterized by a monotonic trend in ε when the Laplace number is high enough.

V. CONCLUSIONS

The capillary instability of a liquid-lined tube has been studied to model the airway closure in human lungs. When the size of the airway diameter becomes very small, e.g., at ninth or tenth branching generation, the dynamics of the thin liquid film lining the airway is dominated by surface tension forces and, when the initial liquid film thickness exceeds a critical value, it may undergo a Plateau-Rayleigh instability which closes the airway within one breathing cycle. This gives rise to a liquid plug.

In our study we are able to address the entire closure process, expanding beyond the limitations of the previous investigations. We carry out a numerical study based on the discretization of the Navier-Stokes system by means of finite volume method (FVM) coupled with a volume of fluid (VOF) method to simulate both liquid and gaseous phases.

Following the conceptual approach of Tai *et al.* [38], the annular film which coats the pipe walls is modeled as a Newtonian fluid whose properties are derived by a homogenization process which involves the multilayer liquid formed by mucus and serous. A validation of our simulations has demonstrated excellent agreement with the experimental results of Bian *et al.* [37], in terms of wall stresses, flow velocities, and tracking of the liquid-gas interface. Both the pre- and the postcoalescence phase have been well reproduced. The radial velocities at the bulge tip dominate before closure, whereas the axial velocity components overshadow the radial motion after coalescence, leading to a quick plug formation and a very quick compression of the menisci on the pipe wall. This is what we termed *bifrontal plug growth*. Indeed, the postcoalescence phase is conceptually similar to the receding of two air fingers, but even though the receding of an air finger has been extensively studied in literature, the significance of our study results from being able to simulate the entire closure process including the sharp topological change observed after the coalescence. In fact, the shear stresses experiences a postcoalescence peak directly correlated to the bifrontal plug growth.

Being confident of the rigorous validation of our simulations against the experimental data, our investigation sheds significant light on the process, with a major focus on the effect of surface tension, liquid flow viscosity, and film thickness on the stresses and their gradients over the airway wall. A batch of 18 simulations is performed to investigate typical conditions of airway closure occurring at the ninth or tenth generation in adult human lungs. Epithelial cells cover the airway wall, and they normally have a characteristic length of $40 \mu\text{m}$. Their injury is therefore induced primarily by shear stress and gradients of normal and tangential stresses along the pipe wall. Quantifying the stress level over the airway wall is the main concern of our study, which proved that the high stress level resulting from the closure of the airway induces serious deformations of the epithelial cells with a consequent damage which has, most likely, a lethal effect for the cells. This scenario has been speculated upon in Ref. [38] for a single set of parameters and three initial film thicknesses, but the quantification of the actual stress level on cells during the whole pre- and postcoalescence process has never been reported before to our knowledge. With our study we demonstrate that wall normal and tangential stresses on the cells, together with their gradients, reach values of $\max_{t,z}(|\tau_w|) \approx 250 \text{ dyn cm}^{-2}$ (300%–600% of the precoalescence values), $\max_{t,z}(|\partial_z p_w|) \approx 4.50 \times 10^4 \text{ dyn cm}^{-3}$ and $\max_{t,z}(|\partial_z \tau_w|) \approx 8 \times 10^3 \text{ dyn cm}^{-3}$ for parameters of typical interest in airways for adult lungs, i.e., $\text{La} = 200$, $\mu = 1.5 \times 10^{-3}$, $\rho = 10^{-3}$, $\lambda = 6$, and $\varepsilon = 0.20$. These levels of stress are much higher than what required for severely damaging the epithelial cells; indeed, according to the experimental results of Bilek *et al.* [51], the cell damage occurs if $\max_{t,z}(|\tau_w|) > 12.9 \text{ dyn cm}^{-2}$, $\max_{t,z}(|\partial_z \tau_w|) > 2.1 \times 10^3 \text{ dyn cm}^{-3}$, and $\max_{t,z}(|\partial_z p_w|) > 3.21 \times 10^4 \text{ dyn cm}^{-3}$. Moreover, an additional confirmation of the lethal effect that wall stresses might have on epithelial cells is reported in Huh *et al.* [52], where it is stated that a dangerous condition for the cells occurs when the shear stress crosses the values of $\max_{t,z}(|\tau_w|) > 98.58 \text{ dyn cm}^{-2}$. This dangerous threshold is less than half of the peak value of the tangential stresses predicted in our airway closure model. Comparing with the experimentally estimated damaging conditions, Tai *et al.* [38] concluded that the level of shear stress in the precoalescence process might be large enough to damage the cells, but pressure and gradients are smaller than the experimentally determined threshold values. With our simulations we proved that the peaks in wall stresses and their gradients occur in the postcoalescence phase, and they are far beyond the damaging thresholds experimentally established. Table III reports a detailed quantification of the level of stress in all the 18 cases we simulated.

The effect of surface tension, liquid dynamic viscosity and initial thickness of the liquid film has been investigated for the parameters listed in Table II. Under the creeping-flow limit, a change in surface tension is inversely proportional to the dimensional closure time and, in our scaling, has no influence on the nondimensional closure time since we employ σ to scale t . However, when inertial terms are taken into account in the momentum equation, increasing the surface tension linearly increases the Laplace number and, consequently, the inertia of the flow. Still, in dimensional quantities, an increase of σ implies a quicker closure. However, in nondimensional time units, the closure of the airway is postponed, proving that the dependence of t_c on σ is slightly sublinear. The major effect of σ is observed for the nondimensional wall pressure gradient, which may experience a qualitative change and, in general, tends to monotonically grow if the Laplace number is small enough.

If instead of changing the surface tension, one considers a different dynamic viscosity of the lining liquid, the effect on the nondimensional groups which control the flow is quadratically observed in La and linearly in the gas-to-liquid viscosity ratio μ . The decrease of one order of magnitude in μ_L produces a strong increase of inertia and of relative viscous forces from the air phase. In nondimensional terms, a delay of the closure event is then observed, associated with an increase of wall shear stresses and stress gradients, whereas the excursion of the normal stresses along the walls Δp_w tends to decrease. Still, in dimensional terms, increasing the liquid viscosity postpones the airway closure.

Finally, an increase of the initial film thickness ε , speeds up the formation of a liquid plug, as predicted in Refs. [37,38]. Moreover, even if tangential and normal wall stresses, as well as shear stress gradients, are more or less insensitive to ε , the initial film thickness has a strong influence on

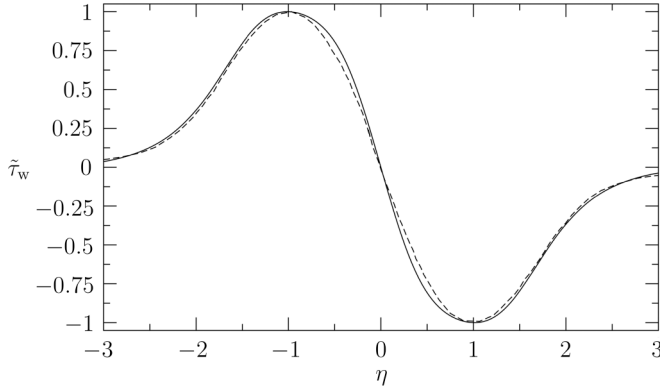


FIG. 13. Normalized wall shear stress $\tilde{\tau}_w = \tau_w / \max(\tau_w)$ at $t = t_s$ against the normalized coordinate $\eta = z/z_{\tau_w, \max}$. The present results (solid line) are compared to the results in Ref. [38] (dashed line).

the wall pressure gradient which increases dramatically when ε decreases. This is a notable feature of the bifrontal plug growth reported in our study.

ACKNOWLEDGMENT

Support from the National Institutes of Health (NIH), Grant No. R01-HL136141, is kindly acknowledged.

APPENDIX

Besides the comparison with the experimental measurements, two additional validation tests are carried out. We first validate our solver comparing its results with the ones reported in Ref. [38]. Figure 13 depicts the normalized wall shear stress $\tilde{\tau}_w = \tau_w / \max(\tau_w)$ right before closure at $t = t_s$ against the normalized coordinate $\eta = z/z_{\tau_w, \max}$. The dashed line refers to the results of Fig. 9(b) in Ref. [38], whereas the solid line depicts our results. The two curves compare very well.

To further validate the numerical solver, we compare it with the finite-difference front-tracking code employed in Ref. [55] using the same computational grid. Figure 14 compares their results

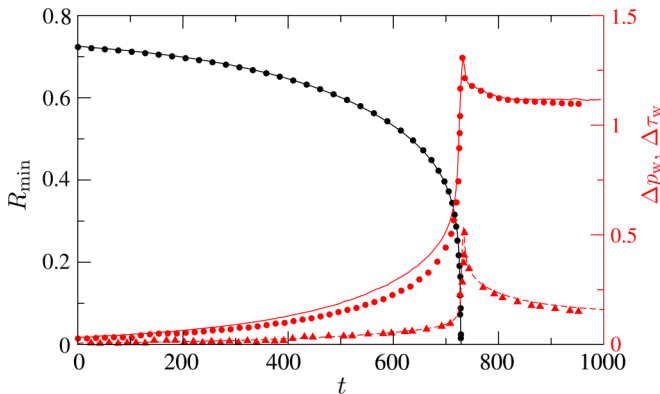


FIG. 14. Minimum of the interface radial location $R_{\min} = \min(R_I)$, excursions of wall pressure $\Delta p_w = \max(p_w) - \min(p_w)$ and shear stress $\Delta \tau_w = \max(\tau_w) - \min(\tau_w)$ computed with BASILISK (lines) and with the numerical solver of Ref. [55] (markers). The nondimensional groups are $La = 100$, $\lambda = 6$, and $\varepsilon = 0.25$.

in terms of R_{\min} , Δp_w , and $\Delta \tau_w$ for $La = 100$, $\lambda = 6$, and $\varepsilon = 0.25$. The closure time predicted by BASILISK is $t_c^{FV/VOF} = 727$, whereas the solver of Ref. [55] computes $t_c^{FD/FT} = 745$, resulting in a relative deviation of about 2%. This deviation is well explained by the different viscosity and density ratio employed when simulating the airway closure with the code of Ref. [55]. Owing to numerical limitations, $\mu = 1/50$ and $\varrho = 1/100$ are employed in the finite-difference or front-tracking code, which led to a slightly slower airway closure. Hence, to ease the comparison for R_{\min} , Δp_w and $\Delta \tau_w$, the results of the finite-difference or front-tracking method are shifted in time of $\Delta t = t_c^{FV/VOF} - t_c^{FD/FT} = -18$. The agreement between the two sets of results is very good. Since BASILISK (lines) employs a finite-volume or volume-of-fluid method, whereas the code of Ref. [55] (markers) uses a finite-difference or front-tracking method, we conclude that the results discussed in our study can be considered independent of the numerical methodology used to compute them.

-
- [1] I. A. Greaves, J. Hildebrandt, and J. F. G. Hoppin, *Micromechanics of the Lung* (American Physiological Society, Rockville, MD, 1986), Vol. 3.
 - [2] P. T. Macklem, D. F. Proctor, and J. C. Hogg, The stability of peripheral airways, *Respir. Physiol.* **8**, 191 (1970).
 - [3] A. B. H. Crawford, D. J. Cotton, M. Paiva, and L. A. Engel, Effect of airway closure on ventilation distribution, *J. Appl. Physiol.* **66**, 2511 (1989).
 - [4] J. Veen, A. J. Beekman, E. H. Bel, and P. J. Sterk, Recurrent exacerbations in severe asthma are associated with enhanced airway closure during stable episodes, *Am. J. Respir. Crit. Care* **161**, 1902 (2000).
 - [5] A. Gunther, C. Siebert, R. Schmidt, S. Ziegler, F. Grimminger, M. Yabut, B. Temmesfeld, D. Walmrath, H. Morr, and W. Seeger, Surfactant alterations in severe pneumonia, acute respiratory distress syndrome, and cardiogenic lung edema, *Am. J. Respir. Crit. Care* **153**, 176 (1996).
 - [6] P. A. Dargaville, M. South, and P. N. McDougall, Surfactant abnormalities in infants with severe viral bronchiolitis, *Arch. Dis. Child.* **75**, 133 (1996).
 - [7] M. Griese, R. Essl, R. Schmidt, E. Rietschel, F. Ratjen, M. Ballmann, and K. Paul, Pulmonary surfactant, lung function, and endobronchial inflammation in cystic fibrosis, *Am. J. Respir. Crit. Care* **170**, 1000 (2004).
 - [8] C. Guerin, S. Lemasson, R. de Varax, J. Milic-Emili, and G. Fournier, Small airway closure and positive end-expiratory pressure in mechanically ventilated patients with chronic obstructive pulmonary disease, *Am. J. Respir. Crit. Care* **155**, 1949 (1997).
 - [9] C. S. Baker, T. W. Evans, B. J. Randle, and P. L. Haslam, Damage to surfactant-specific protein in acute respiratory distress syndrome, *Lancet* **353**, 1232 (1999).
 - [10] F. R. Bode, J. Dosman, R. R. Martin, H. Ghezzi, and P. T. Macklem, Age and sex differences in lung elasticity, and in closing capacity in nonsmokers, *J. Appl. Physiol.* **41**, 129 (1976).
 - [11] G. B. Drummond and J. Milic-Emili, Forty years of closing volume, *Br. J. Anaesth.* **99**, 772 (2007).
 - [12] G. K. Prisk, H. J. Guy, A. R. Elliott, M. Paiva, and J. B. West, Ventilatory inhomogeneity determined from multiple-breath washouts during sustained microgravity on Spacelab SLS-1, *J. Appl. Physiol.* **78**, 597 (1995).
 - [13] J. B. West, A. R. Elliott, H. J. Guy, and G. K. Prisk, Pulmonary function in space, *JAMA* **277**, 1957 (1997).
 - [14] J. B. Grotberg, Respiratory fluid mechanics and transport processes, *Ann. Rev. Biomed. Eng.* **3**, 421 (2001).
 - [15] P. A. Gauglitz and C. J. Radke, An extended evolution equation for liquid film breakup in cylindrical capillaries, *Chem. Eng. Sci.* **43**, 1457 (1988).
 - [16] M. Liu, L. Wang, E. Li, and G. Enhorning, Pulmonary surfactant will secure free airflow through a narrow tube, *J. Appl. Physiol.* **71**, 742 (1991).

- [17] K. J. Cassidy, Liquid film dynamics in the pulmonary airways, Ph.D. thesis, Northwestern University (1999).
- [18] D. Halpern and J. B. Grotberg, Surfactant effects on fluid-elastic instabilities of liquid-lined flexible tubes: A model of airway closure, *J. Biomech. Eng.* **115**, 271 (1993).
- [19] D. Campana, J. Di Paolo, and F. A. Saita, A 2-D model of Rayleigh instability in capillary tubes—Surfactant effects, *Int. J. Multiphase Flow* **30**, 431 (2004).
- [20] D. Halpern, H. Fujioka, and J. B. Grotberg, The effect of viscoelasticity on the stability of a pulmonary airway liquid layer, *Phys. Fluids* **22**, 011901 (2010).
- [21] D. Halpern and J. B. Grotberg, Fluid-elastic instabilities of liquid-lined flexible tubes, *J. Fluid Mech.* **244**, 615 (1992).
- [22] M. Heil, A. L. Hazel, and J. A. Smith, The mechanics of airway closure, *Respir. Physiol. Neurobiol.* **163**, 214 (2008).
- [23] D. Halpern and J. B. Grotberg, Nonlinear saturation of the Rayleigh instability due to oscillatory flow in a liquid-lined tube, *J. Fluid Mech.* **492**, 251 (2003).
- [24] X. Zhang, R. Padgett, and O. Basaran, Nonlinear deformation and breakup of stretching liquid bridges, *J. Fluid Mech.* **329**, 207 (1996).
- [25] D. T. Papageorgiou, On the breakup of viscous liquid threads, *Phys. Fluids* **7**, 1529 (1995).
- [26] J. Eggers and E. Villermaux, Physics of liquid jets, *Rep. Prog. Phys.* **71**, 036601 (2008).
- [27] Lord Rayleigh, On the instability of cylindrical fluid surfaces, *Philos. Mag.* **34**, 177 (1892).
- [28] S. L. Goren, The instability of an annular thread of fluid, *J. Fluid Mech.* **12**, 309 (1962).
- [29] M. Johnson, R. D. Kamm, L. W. Ho, A. Shapiro, and T. J. Pedley, The nonlinear growth of surface-tension-driven instabilities of a thin annular film, *J. Fluid Mech.* **233**, 141 (1991).
- [30] V. Duclaux, C. Clanet, and D. Qu  e, The effects of gravity on the capillary instability in tubes, *J. Fluid Mech.* **556**, 217 (2006).
- [31] L. A. Newhouse and C. Pozrikidis, The capillary instability of annular layers and liquid threads, *J. Fluid Mech.* **242**, 193 (1992).
- [32] G. F. Dietze and C. Ruyer-Quil, Films in narrow tubes, *J. Fluid Mech.* **762**, 68 (2015).
- [33] J. B. Grotberg, Pulmonary flow and transport phenomena, *Ann. Rev. Fluid Mech.* **26**, 529 (1994).
- [34] S. N. Ghadiali and D. P. Gaver, Biomechanics of liquid-epithelium interactions in pulmonary airways, *Respir. Physiol. Neurobiol.* **163**, 232 (2008).
- [35] J. B. Grotberg, Respiratory fluid mechanics, *Phys. Fluids* **23**, 021301 (2011).
- [36] J. B. Grotberg, Crackles and wheezes: Agents of injury? *Ann. Am. Thorac. Soc.* **16**, 967 (2019).
- [37] S. Bian, C. F. Tai, D. Halpern, Y. Zheng, and J. B. Grotberg, Experimental study of flow fields in an airway closure model, *J. Fluid Mech.* **647**, 391 (2010).
- [38] C. F. Tai, S. Bian, D. Halpern, Y. Zheng, M. Filoche, and J. B. Grotberg, Numerical study of flow fields in an airway closure model, *J. Fluid Mech.* **677**, 483 (2011).
- [39] G. Tryggvason, R. Scardovelli, and S. Zaleski, *Direct Numerical Simulations of Gas-Liquid Multiphase Flows* (Cambridge University Press, Cambridge, 2011).
- [40] S. Popinet, Numerical models of surface tension, *Ann. Rev. Fluid Mech.* **50**, 49 (2018).
- [41] S. Popinet, Basilisk, <http://basilisk.fr> (2014).
- [42] J. B. Bell, P. Colella, and H. M. Glaz, A second-order projection method for the incompressible Navier-Stokes equations, *J. Comput. Phys.* **85**, 257 (1989).
- [43] S. Popinet, Gerris: A tree-based adaptive solver for the incompressible Euler equations in complex geometries, *J. Comput. Phys.* **190**, 572 (2003).
- [44] S. Popinet, An accurate adaptive solver for surface-tension-driven interfacial flows, *J. Comput. Phys.* **228**, 5838 (2008).
- [45] R. Scardovelli and S. Zaleski, Direct numerical simulation of free-surface and interfacial flow, *Ann. Rev. Fluid Mech.* **31**, 567 (1999).
- [46] E. Aulisa, S. Manservigi, and R. Scardovelli, A novel representation of the surface tension force for two-phase flow with reduced spurious currents, *Comput. Methods Appl. Mech. Eng.* **195**, 6239 (2006).
- [47] J. Brackbill, D. B. Kothe, and C. Zemach, A continuum method for modeling surface tension, *J. Comput. Phys.* **100**, 335 (1992).

- [48] R. G. Crystal, *The Lung: Scientific Foundations* (Lippincott, New York, 1997).
- [49] S. K. Lai, Y.-Y. Wang, D. Wirtz, and J. Hanes, Micro- and macrorheology of mucus, *Adv. Drug Delivery Rev.* **61**, 86 (2009).
- [50] N. J. Douville, P. Zamankhan, Y.-C. Tung, R. Li, B. L. Vaughan, C.-F. Tai, J. White, P. J. Christensen, J. B. Grotberg, and S. Takayama, Combination of fluid and solid mechanical stresses contribute to cell death and detachment in a microfluidic alveolar model, *Lab Chip* **11**, 609 (2011).
- [51] A. M. Bilek, K. C. Dee, and D. P. Gaver, Mechanisms of surface-tension-induced epithelial cell damage in a model of pulmonary airway reopening, *J. Appl. Physiol.* **94**, 770 (2003).
- [52] D. Huh, H. Fujioka, Y. C. Tung, N. Futai, R. Paine, J. B. Grotberg, and S. Takayama, Acoustically detectable cellular-level lung injury induced by fluid mechanical stresses in microfluidic airway systems, *Proc. Natl. Acad. Sci. USA* **104**, 18886 (2007).
- [53] E. Georgiou, D. T. Papageorgiou, C. Maldarelli, and D. S. Rumschitzki, The double layer–capillary stability of an annular electrolyte fluid surrounding a dielectric-fluid core in a tube, *J. Fluid Mech.* **226**, 149 (1991).
- [54] E. A. Hassan, E. Uzgoren, H. Fujioka, J. B. Grotberg, and W. Shyy, Adaptive Lagrangian-Eulerian computation of propagation and rupture of a liquid plug in a tube, *Int. J. Num. Meth. Fluids* **67**, 1373 (2011).
- [55] M. Muradoglu, F. Romanò, H. Fujioka, and J. B. Grotberg, Effects of surfactant on propagation and rupture of a liquid plug in a tube, *J. Fluid Mech.* **872**, 407 (2019).